

We are IntechOpen, the world's leading publisher of Open Access books Built by scientists, for scientists

4,800

Open access books available

122,000

International authors and editors

135M

Downloads

Our authors are among the

154

Countries delivered to

TOP 1%

most cited scientists

12.2%

Contributors from top 500 universities



WEB OF SCIENCE™

Selection of our books indexed in the Book Citation Index
in Web of Science™ Core Collection (BKCI)

Interested in publishing with us?
Contact book.department@intechopen.com

Numbers displayed above are based on latest data collected.
For more information visit www.intechopen.com



GNSS High-Rate Data and the Efficiency of Ionospheric Scintillation Indices

*Vladislav V. Demyanov, Maria A. Sergeeva
and Anna S. Yasyukevich*

Abstract

The work discusses the efficiency of different ionospheric scintillation indices. The new index D2fi based on the GNSS carrier phase observable was introduced. We analyze the accuracy of the phase measurements, in particular its dependence on the GNSS equipment thermal noises, multipath and external noises, and presettings of Phase Lock Loop and Code Delay Discriminator. The performance of DROTI, $S4$, $\sigma\phi$, and D2fi was considered for the case of high-rate data. The “sensitivity” and reliability of each index differs significantly and depends on the time resolution of the carrier phase data. The new index D2fi advantages are that it is easily derived and has a clear dependence on GNSS hardware and software features. D2fi was proven to be a useful tool to detect the small-scale ionospheric disturbances based on high-rate GPS carrier phase measurements.

Keywords: GPS, ionospheric scintillation indices, high-rate GNSS data

1. Introduction

GNSS data with high-rate sampling becomes more and more available worldwide [1, 2]. It provides opportunities for the better results in the field of ionospheric scintillation research. Standard ionospheric indices and parameters $S4$, $\sigma\phi$, and $ROTI$ -based indices and ionospheric total electron (TEC) are widely used for the ionospheric research as reliable and informative tools [3–6]. Unfortunately, their accuracy, efficiency, and reliability depend on the integration time, input data sampling rate, and de-trending and filtering procedures of the carrier phase time series [7–9]. GNSS hardware architecture, Code Delay Discriminator (CDD), and Phase Lock Loop (PLL) presets play the crucial role in the carrier phase measurement quality especially under multipath environment conditions [10, 11]. The mentioned issues bring uncertainties to the ionospheric indices calculations which, in turn, can degrade the experimental results interpretation. The sensitivity of the ionospheric indices/parameters depends on the time resolution of input data. One of the important questions is whether the data rate is high enough to be sure that all the necessary ionospheric information is derived. There are different works on GPS scintillation, for instance, [1, 7, 12], but still there is a room for the more profound analysis of the data of higher time resolution than 10 Hz. Such a high-rate data is often considered as a noise but it is not exactly the truth. The excellent results by [1]

based on the amplitude and phase measurements with the data rate of 100 Hz demonstrated the new opportunity to look at, and far beyond, 10 Hz resolution. The ionospheric scintillations show different features at different GNSS frequencies. Hence, the single-frequency carrier phase measurements can be involved for more informative analysis. The final accuracy of the carrier phase measurements depends on the GNSS equipment internal noises, multipath, and external noises. Incorrect presettings of PLL and CDD as well as the bad quality of reference oscillator can mislead a researcher in his or her final conclusions. To mitigate the impact of the mentioned factors, it is necessary to preset the receiver hardware (including antenna, preamplifier, and inter-frequency filter) and software (PLL and CDD types and parameters).

It is important to find such an ionospheric scintillation index which is easily derived and has a clear dependence on both the ionospheric turbulence structure and GNSS hardware and software presets. In this work, the second-order derivative of the GPS signal carrier phase based on high-rate carrier phase time series is suggested as a promising means for the ionospheric scintillation detection. No additional complex processing is needed to obtain this new scintillation index.

The work [1] and the general necessity to define the GPS data time resolution sufficient for the robust scintillation analysis were the motivation for the authors to test the real sensitivity of the ionospheric indices depending on the input data sampling rate. We consider GNSS carrier phase observable to be the most capable of observing the ionospheric disturbances and scintillations. The aims of this study include (a) introduction of the new index that is the second-order derivative of the GPS signal carrier phase (D2fi index) which helps to reveal scintillation events; (b) test of sensitivity of D2fi, DROTI, S4, and $\sigma\phi$ indices based on 50 Hz GPS data; and (c) consideration of the benefits and limitations of these indices for scintillation studies. The analysis was performed for the case study and was based on GPS data of the mid-latitude GNSS station located near Irkutsk, Russia, during the intense geomagnetic storm.

2. The carrier phase noise content at the phase lock loop input

Ionospheric phase scintillations are induced with ionospheric irregularities of hundreds of meters to several kilometer size. These irregularities correspond to the Fresnel frequencies from ≈ 0.1 to ≈ 10 Hz [13, 14]. According to [1, 2, 15], it is possible to detect small-scale ionospheric irregularities of hundreds of meters to several kilometer size by observing not only the fast carrier phase variations but also the carrier phase noise variations which were considered earlier as “noise” [1]. This is possible if the data sampling rate is high enough to exclude low-frequency variations and trends from the carrier phase time series. The data sampling rate should contain the sufficient ionospheric information. The authors [1] showed that the majority of the phase scintillation events can be revealed if data sampling rate between 10 and 40 Hz is used. Therefore, for the analysis of weak ionospheric scintillations, the sampling data rate higher than 10 Hz should be used.

To extract the phase noise variations from the complex carrier phase data, we use the carrier phase derivatives. The second-order derivative works as a high-pass filter and removes the phase ambiguity, all the low-frequency trends (due to the relative motion between satellite and receivers), multipath slow variations, and low-frequency phase variations due to reference oscillator frequency drift. It allows us to extract the phase noise variations from the phase measurements without additional complex processing procedures. The carrier phase noise derivative can be also used as a new parameter in GPS occultation technology [16].

Let us estimate the values of the main components of the carrier phase noise. They should be small enough to obtain the pure ionospheric phase scintillation based on the D2fi index. In case of the stationary receiver, there are no phase variations and phase measurement noises due to vibration and jerks. Based on this assumption, the noise error in carrier phase measurements depends on two main factors: the carrier-to-noise ratio at the PLL input and the multipath noises at the reception point.

For an ideal PLL without inner loss, the noise dispersion of phase measurements is determined as follows [17]:

$$\sigma_{\varphi}^2 = \frac{1}{(2\pi)^2} \cdot \frac{\Delta F_{PLL}}{2 \cdot CN_0} \quad (1)$$

where ΔF_{PLL} is the noise bandwidth of the PLL filter (Hz) and CN_0 is the carrier-to-noise ratio at the PLL unit input (dBW).

Thus, the noise level of the carrier phase measurements is determined by the carrier-to-noise ratio (CNR) at the PLL input. The CNR depends on (1) the level of external noises, (2) the antenna pattern, and (3) the low-noise preamplifier (LPA) gain. In addition to external noise, the inherit receiver thermal noise, the short-term instability of the reference oscillator, the signal sampling, and quantization noise should be considered as well.

According to expression (1), the final accuracy of the carrier phase measurements depends on the filter noise bandwidth. At the same time, the carrier-to-noise ratio at the PLL input depends on the time of accumulation of instantaneous phase measurement samples. Thus, the noise dispersion of phase measurements can be determined more precisely as follows [17]:

$$\sigma_{\varphi} = \frac{1}{(2\pi)^2} \cdot \sqrt{\sigma_T^2 + \sigma_F^2} \quad (2)$$

where σ_T^2 is the dispersion of receiver thermal noise and σ_F^2 is the dispersion of noise caused by the Allan deviation.

The noise components of the phase measurements with dispersions σ_T^2 and σ_F^2 depend on the above factors as follows [17]:

$$\sigma_T = \frac{1}{2\pi} \cdot \sqrt{\frac{\Delta F_{PLL}}{CN_0} \cdot \left(1 + \frac{1}{2T_{COR} \cdot CN_0}\right)} \quad (3)$$

$$\sigma_F = m \cdot \frac{\sigma_F(\tau) \cdot f}{\Delta F_{PLL}} \quad (4)$$

where T_{COR} is the time of accumulation of instantaneous phase measurement samples (ms), $\sigma_F(\tau)$ is the RMS of the short-term instability of the reference generator frequency (Hz), f is the signal carrier frequency, and m is a coefficient depending on the PLL filter type ($m = 144$ for a second-order PLL filter and $m = 160$ for a third-order PLL filter).

The carrier-to-noise ratio at the PLL input is a function of the receiver noise temperature (including the antenna), as well as the environment noise temperature (the Earth noise, the total noise of cosmic radio sources, and the Sun noise). The measurements of noise caused by analog-to-digital signal conversion, as well as signal-to-noise level with regard to filtering, amplification, and antenna gain, can be expressed through the corresponding loss in the resulting carrier-to-noise ratio at the phase detector input. Therefore, the carrier-to-noise ratio at the PLL input can be expressed as follows [17]:

$$CN_0 = P_{rec} + G_A - N_T - L_{tr} - L_{dg} \quad (5)$$

where P_{rec} is the signal level at the receiving point (dBW); G_A is the antenna gain (dB); N_T is the spectral density of the receiver thermal noise power (dBW); L_{tr} is the total power loss during filtering, frequency conversion, and the signal attenuation in the cable (dB); and L_{dg} is the signal power loss due to its analog-to-digital conversion (dB).

According to formula (5), two factors affecting the carrier-to-noise ratio at the PLL input can be deduced. The first factor is constant during the measurement and depends on the receiver equipment type. It is defined by the L_{tr} , L_{dg} , and G_A values. These typical values are $L_{tr} = -2 \dots -4$ dB, $L_{dg} = -0.55 \dots -3.0$ dB, and $G_A = -2 \dots -7.5$ dB (depending on the satellite line-of-site angular direction) [18].

At the same time, there is a factor that depends not only on the equipment type but also changes randomly. This is the receiver thermal noise N_T . Let us estimate its change limits and reveal the most significant causes that affect the magnitude of this noise. The spectral power of the thermal noise is related to the temperature of medium [18]:

$$N_T = 10 \cdot \lg(K \cdot T_\Sigma) \quad (6)$$

where $K = 1.38 \cdot 10^{-23}$ (W·s/K) is the Boltzmann constant and T_Σ is the total noise temperature of the equipment and the external environment, forming measurement noise.

The total noise temperature can be estimated as follows [18]:

$$T_\Sigma = T_{EXN} + T_A + T_{LPA} \quad (7)$$

where T_{EXN} is external noise due to the Earth noise (T_{EN}), the noise of the Galaxy and cosmic radio sources (T_{CN}), and the Sun noise (T_{SN}); T_A is the antenna noise temperature caused by the active loss resistance noise in the antenna; and T_{LPA} is the noise temperature of a low-noise preamplifier.

Under standard physical conditions, the Earth noise temperature is $T_{\Sigma,EN} = 300K$. The Earth noise component, which is present at the PLL input ($T_{\Sigma,EN}$), is determined by the antenna pattern as follows [18]:

$$T_{EN} = 100 \cdot \left(\frac{\beta}{2\theta}\right)^2 \cdot T_{\Sigma,EN} \quad (8)$$

where $\frac{\beta}{2\theta}$ is the ratio of the angular aperture of a groundward part of the antenna pattern, with respect to the total angular aperture of the antenna pattern.

According to Eq. (8), the higher the $\frac{\beta}{2\theta}$ ratio, the higher the magnitude of the Earth noise. With regard to the known antenna pattern of typical navigation receiver antennas, the value $\left(\frac{\beta}{2\theta}\right)^2$ can be within 0.004–0.01 [18]. Thus, the Earth noise temperature at the PLL input is $T_{EN} = 1.2\text{--}3$ K, and the correspondent noise spectral power varies from -227.8 to -223.8 dBW/Hz.

Similarly, the Sun noise temperature can be obtained. The total noise temperature of the Sun is $T_{\Sigma,S} = 6000K$. The angular size of the Sun visible from the Earth's surface is $\beta_C = 0,5^\circ$. Considering the above mentioned typical antenna pattern, the $\left(\frac{\beta}{2\theta}\right)^2$ ratio is about 10^{-5} . When the sunlight falls into the antenna aperture, the Sun noise temperature $T_{SN} = 0,00001 \times 6000 \approx 0,06$ K. This corresponds to the Sun noise temperature at the PLL input of about -241 dBW/Hz.

The sky noise temperature (T_{CN}), including all cosmic radio noise sources, can be considered equal to 100 K [18]. This noise is accepted for the entire antenna aperture. If we consider an ideal antenna without losses, the corresponding sky noise power at the PLL input is about -208 dBW/Hz.

The inherit antenna noise temperature T_A results from the noise of active loss resistance in the antenna [18]:

$$T_A = T_0 \cdot (1 - \eta) \quad (9)$$

where T_0 is the antenna physical temperature and η is the antenna efficiency.

If the antenna temperature is equal to 300 K and the typical antenna efficiency is between 80 and 90%, the temperature $T_A \approx 60 \dots 30$ K and the corresponding antenna noise power is between -211 and -214 dBW/Hz.

The noise temperature of the preamplifier is defined as follows [18]:

$$T_{LPA} = T_{01} \cdot (\varepsilon - 1) \quad (10)$$

where ε is the preamplifier noise coefficient and T_{01} is the receiver physical temperature. Let us assume that the typical noise coefficient for the modern preamplifiers varies from 1.4 to 2 dB and T_{01} is 300 K. These conditions result in $T_{LNA} \approx 120 \dots 300$ K, and the corresponding thermal noise power is from -204 to -208 dBW/Hz.

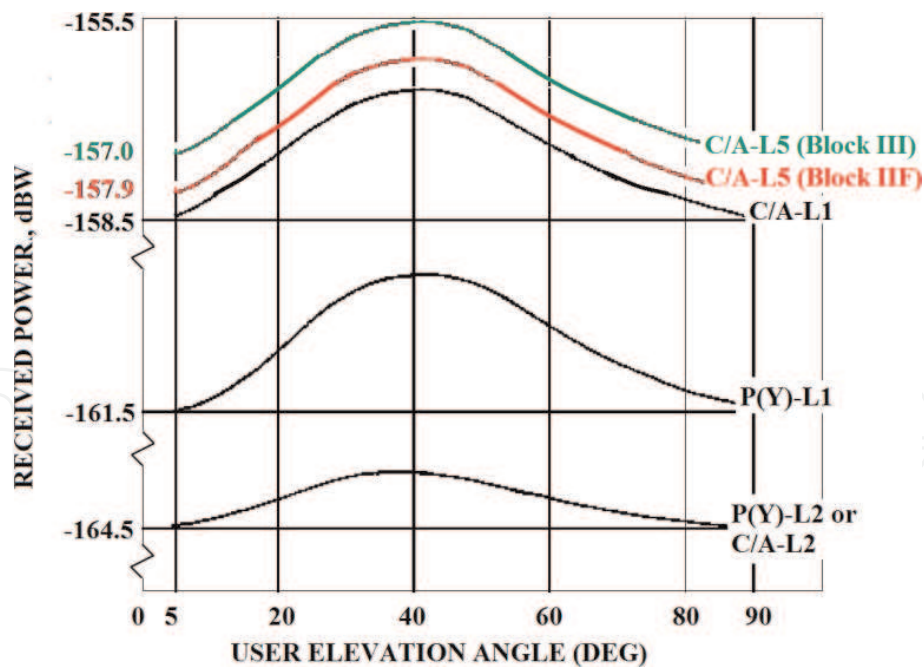
Table 1 shows the values of noise temperatures and noise spectral power for the above mentioned components of the receiver thermal noise (N_T) and external noises. According to the table, the thermal noise at the PLL input significantly depends on the receiver hardware and the antenna pattern. This can result in the significantly different carrier phase measurements accuracy and noise level when using navigation receivers and antennas of various types and models.

Using the information from the **Table 1** and formulas (2)–(5), we can estimate the noise level of the phase measurements in a stationary receiver when measuring the phase at different GPS frequencies and satellite elevations. Let us assume that $\Delta F_{PLL} = 18\text{Hz}$, accumulation time $T_{COR} = 20\text{mc}$, Allan deviation of the reference generator $\sigma_F(\tau) = 10^{-11}$, the maximum and minimum power levels of the signals (P_{rec}), received at L1, L2 and L5 frequencies are described by curves in **Figure 1** [19, 20]. The values of the standard deviation of the phase noise for this case are given in **Table 2**.

The quality of the receiver radio-frequency chain (RFC) and the regular variations in the signal level at the reception point play an important role in the potential accuracy of the signal phase measurements. In particular, the sustainable phase tracking threshold equals 15° [17] is almost reached under conditions of the worst radio-frequency chain parameters (**Table 2**) and the minimum signal receiving

Noise source	Noise temperature, K	Power spectral density dBW/Hz
Preamplifier noise	120 ... 300	$-204 \dots -208$
Antenna noise	30 ... 60	$-214 \dots -211$
Sky noise (all sources)	100	-208
Earth noise	1.2 ... 3	$-228 \dots -224$
Sun noise	0.06	-241
Total value	251.26 ... 463.06	$-204.6 \dots -202.1$

Table 1.
 The receiver and external thermal noises.


Figure 1.

The power levels of signals received by a linearly polarized antenna with 3dBi antenna gain at L1, L2, and L5 GPS frequencies (the curves were reconstructed based on [19, 20]).

Frequency, MHz	Minimal value σ_φ , deg	Maximal value σ_φ , deg
L1 = 1575.42	1.59	7.22
L2 = 1227.60	3.35	14.85
L5 = 1176.45	1.33	6.06

Table 2.

Noise values of phase measurements.

level at the L2 frequency. Thus, although the phase measurements yield the best accuracy for ionospheric scintillation detection, still the careful presetting of GNSS receiver hardware and the consideration of measurement conditions are needed. To note, under the similar conditions, the best accuracy of the phase measurements is achieved if the signals are used at the L5 GPS frequency. This can be explained by the highest carrier-to-noise ratio in the given measurement channel (**Figure 1**).

Another important factor for the high accuracy of carrier phase measurements is the correct choice of the PLL settings such as accumulation time (T_{COR}) and the PLL filter noise bandwidth (ΔF_{PLL}). It is known that the third-order tracking system has stable and unstable operation zones. If there are no impacts on the navigation receiver in the form of vibrations, jerks, and electromagnetic jammer interference, then the stable tracking of the carrier phase is provided with the following conditions fulfilled [17]:

$$0 < \Delta F_{PLL} < \frac{0.7}{T_{COR}} \quad (11)$$

When using an optimal phase discriminator, the measured parameter (phase) should not be changed during the accumulation time (T_{COR}). In this case, when estimating the phase, it is necessary to head for the longest character of the transmitted message. This is the character of the navigation message, which is transmitted simultaneously with the ranging code on the same carrier frequency. If the

duration of the navigation message character is 20 ms [21], the accumulation of measurements should be $T_{COR} \geq 20$ ms.

The measured parameter is not obligatory constant within T_{COR} interval in case of a quasi-optimal phase discriminator [21]. Therefore, the accumulation time should be within the interval $1ms \leq T_{COR} \leq 20ms$. Here, the ranging code sequence length (1 ms for the CA code) determines the lower limit of the accumulation time (1 ms). The final decision about the optimal T_{COR} value is limited by two factors: (1) the carrier-to-noise ratio in the phase measuring channel and (2) the influence of the low-frequency processes on the phase measurement accuracy. The longer the time interval, the higher both the carrier-to-noise ratio and the phase measurement accuracy. However, with an increase of the accumulation time more than 10–20 ms, the effects of instability in the reference oscillator frequency and Doppler frequency drift can appear [21]. Therefore, it is not appropriate to increase the accumulation time over these limits.

After the determination of the optimal T_{COR} value, the selected PLL noise bandwidth should satisfy Eq. (11). In addition, according to Eq. (1) the noise level of the phase measurement depends on the noise bandwidth ΔF_{PLL} . Therefore, the practical choice of the noise bandwidth depends on the expected measurement conditions and usually lies within the range from 10 to 20 Hz. If there is an impact of external electromagnetic interference, the phase tracking stability reduces. Therefore, the choice of the wider noise bandwidth increases the reliability of the phase tracking. Finally, according to expressions (3) and (4), the increase of the noise bandwidth leads to the proportional increase of the average RMS of the receiver equipment thermal noise. On the other hand, as ΔF_{PLL} increases, the noise component related to the short-term frequency instability of the reference oscillator decreases. Thus, the noise bandwidth can be reduced without the significant loss of the phase measurement quality by using a better-quality reference oscillator.

The multipath effect is another important source of the carrier phase noises. In general, the phase error due to multipath can be calculated as a difference between the carrier phase of the reflected composite signal and the carrier phase of the direct signal. In the presence of multipath propagation, the composite signal phase shifts randomly from the direct signal phase, and the NCO-generated local carrier locks to the composite carrier phase, resulting in the error of the phase measurement. In the case of one reflected signal, the error of the phase measurement is defined as follows [10]:

$$\Delta\Psi = \arctan \left(\frac{\alpha_1 \cdot R(\hat{\tau}_C - \tau_1) \cdot \sin \varphi_1}{R(\hat{\tau}_C) + \alpha_1 \cdot R(\hat{\tau}_C - \tau_1) \cdot \cos \varphi_1} \right) \quad (12)$$

where $R(\hat{\tau}_C)$ is the autocorrelation function of the PRN code, $R(\hat{\tau}_C - \tau_1)$ is the cross-correlation function between the direct GNSS signal and the reflected signal, $\hat{\tau}_C$ is the receiver estimate of the incoming signal code delay, τ_1 is the reflected signal code delay, α_1 is the reflection coefficient that corresponds to the Signal to Multipath Ratio (SMR) as $SMR = 20 \cdot \log(\alpha_1^{-1})$, and φ_1 is the phase of the reflected signal.

If the direct signal has no distortion in the form the PRN code, the autocorrelation function ($R(\hat{\tau}_C)$) depends on the front-end bandwidth of the GNSS receiver radio-frequency chain. The PRN codes have one main lobe and several side lobes in the frequency domain. In practice, the signal is band limited, and only the main lobe and one or more side lobes are used for the signal processing. As a result, the sharp correlation peaks are rounded and the ends are trailed-off. It was found earlier that the RFC bandwidth affects the maximum error value significantly [10, 11]. In the case of the unlimited bandwidth, the misalignment in the $\hat{\tau}_C$ value computation is

zero. In the case of 10 MHz bandwidth, the misalignment is not equal to zero and can vary within $\pm 0.03 t_C$, where t_C is PRN code chip length. The narrower bandwidth of 2 MHz brings the significant misalignment to the calculation of the $\hat{\tau}_C$ value which can reach the values of $\pm (0.1 \dots 0.3) t_C$ [10].

The cross-correlation function $R(\hat{\tau}_C - \tau_1)$ significantly depends on the early-late correlator spacing (d) and PRN code rate. It is well known that the code delay discriminator output ($\Delta_{d,out}$) depends on the correlator spacing time (Td), the input tracking error ($\hat{\tau}_C - \tau_c$), and the PRN code chip length (t_C) as follows [17]:

$$\Delta_{d,out} = -2 \cdot \frac{(\hat{\tau}_C - \tau_c)}{t_C} \quad \tau_e \leq Td \quad (13)$$

This equation describes the discriminator output in case if the input tracking error (τ_e) is within linear part of the discriminator performance. The maximal discriminator output value is limited by the correlator spacing time and depends on the code chip length [17]

$$\Delta_{d,MAX} = 2 \cdot \frac{Td}{t_C} \quad \tau_e = Td \quad (14)$$

Thus, both the correlator spacing and the PRN code chip length define the maximal code tracking error value and, as a result, the cross-correlation function $R(\hat{\tau}_C - \tau_1)$. Let us consider the particular example of L1 C/A code and the coherent discriminator using a standard correlator with the correlator spacing of $Td = \pm 0.5t_C$ and a narrow correlator with the spacing of $Td = \pm 0.1t_C$. The work [10] proved that for this particular case, the maximum and the minimum errors are much higher than the narrow correlator with 0.1 chip spacing. If the correlator spacing is $\pm 0.5t_C$, the code tracking error lies within $\pm 0.4 \dots 0.5 t_C$. It corresponds to the code delay computation error $\hat{\tau}_C = \pm 120 \dots 150$ m for C/A PRN code. In contrast to that, in the case of the narrow correlator, the code tracking error is $\hat{\tau}_C = \pm 25 \dots 30$ m for C/A code.

To estimate the possible impact of the PRN code rate on the multipath error, the multipath error envelopes can be used [22, 23]. **Table 3** illustrates the GPS PRN code characteristics transmitted at L1 and L5 GPS frequencies. **Table 4** was reconstructed based on the results [23]. It illustrates the maximal code multipath error ($\hat{\tau}_C \cdot c$) in relation to the PRN code rate and correlator spacing for the coherent discriminator.

Table 4 shows that the size of the area, where the multipath effect is significant, depends on the code rate or, to be exact, on the PRN chip length (t_c). This is because the discriminator function value varies within $0 < Td < t_c$. If the input code tracking error exceeds t_c , the discriminator function values saturate. Hence, the code discriminator is sensitive within $\pm t_c$. Moreover, in the case of the standard correlator, the multipath error beyond the multipath delay of $1.5 t_c$ can differ from zero. This is due to the fact that the PRN code autocorrelation characteristics has one major peak and many minor peaks [17]. If the reflected signal is received more

Frequency/PRN code	Carrier frequency, MHz	Code rate (Mbps)
L1 C/A	1575.25	1.023
L5 I5, L5 Q5	1176.45	10.23

Table 3.
L1, L2, and L5 GPS signal characteristics [19, 20].

Frequency/PRN code	Maximal code multipath error ($\tau_C \bullet c$), meters		Maximal relative multipath delay ($\tau_1 \bullet c$), meters	
	$Td = \pm 0.5t_C$	$Td = \pm 0.1t_C$	$Td = \pm 0.5t_C$	$Td = \pm 0.1t_C$
L1/CA	39.0	8.0	350	300
L5/I5, L5/Q5	4.0	0.8	40	35

Table 4.

The code multipath error in relation to the relative multipath delay at the fixed SMR = 3 dB and different correlator spacing.

than 1.5 chip delayed, it can cause the minor peak or a non-zero correlation value as well [24]. This effect is not significant for our analysis, thus we will not consider it further.

The maximum error values of the phase measurement due to multipath are calculated according to Eq. (12). It was supposed that there is only one reflected signal that has the phase shift angle $\varphi_{1,max}$, rad and delayed τ_1 seconds. This angle corresponds to the case when the multipath errors reach the maxima and affects the multipath error envelope which contains all the smaller variations of the $\Delta\Psi$ values. The angle $\varphi_{1,max}$ can be found by differentiating Eq. (12) with respect to φ_1 , putting it to zero and solving it for φ_1 . It results in the following [10]:

$$\varphi_{1,max} = \cos^{-1}\left(\frac{-\alpha_1 \cdot R(\hat{\tau}_C - \tau_1)}{R(\hat{\tau}_C)}\right) \quad (15)$$

Figure 2 shows the standard deviations of the carrier phase multipath errors with respect to multipath delays for different SMR using the correlator spacing of $Td = \pm 0.1t_C$ and the coherent discriminator for code tracking. The results in **Figure 2** correspond to L1 C/A PRN code (solid lines) and L5 I5 (Q5) PRN codes (dashed lines). Here, the unlimited RFC bandwidth and τ_1 variations within the range of $\pm t_c$ are supposed. The results are obtained changing the reflected signal relative phase shift by discrete steps of 0.1 of a total phase cycle, calculating the

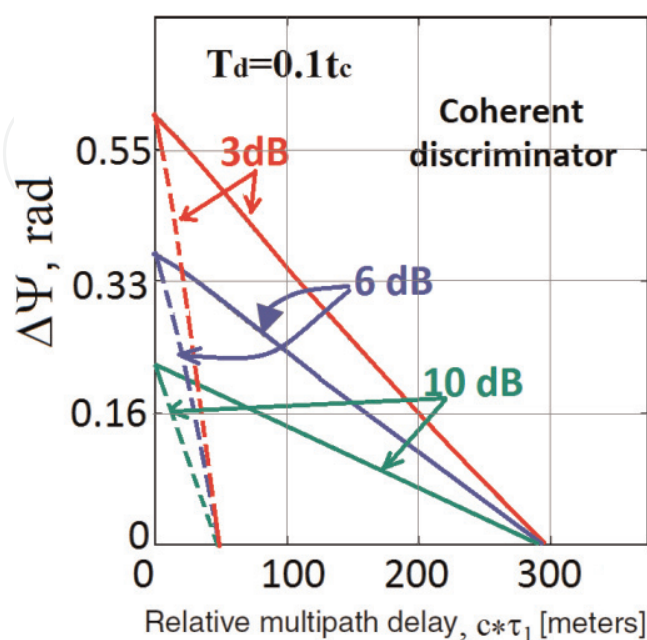


Figure 2.

The multipath error envelopes for L1 C/a (solid lines) and L5 I5 (Q5) PRN codes (dashed lines) in relation to SMR.

multipath error ($\Delta\Psi$) at each step and then taking their mean values and standard deviation.

According to **Figure 2**, there is a dependence of the error on SMR. The magnitude of the multipath error ($\Delta\Psi$) is proportional to the strength of the multipath signal. Moreover, the multipath error value is independent on the carrier wavelength (Eq. 12), but it is mostly a function of the antenna-reflector distance through the correlation function $R(\tau_C - \tau_1)$. If the multipath delay (τ_1) is high, the correlation value decreases and so does the multipath error amplitude. The maximal multipath error in the phase measurement does not exceed 0.6 rad under the above mentioned assumptions (**Figure 2**). However, under real conditions the multipath error is formed as a sum of several reflected signals or as a result of another kind of multipath sources such as diffuse scattering or diffraction. Thus, the higher values of the error of the phase measurement due to multipath can be expected. The authors [10, 11] demonstrated that the maximal value of the error due to multipath does not depend significantly on the code correlator spacing and there is no similar dependence on the code discriminator type as well.

3. Experimental results and analysis

3.1 Indices comparison

This section discusses the performance of the “standard” ionospheric scintillation indices and the index D2fi based on high-rate sampling data. The D2fi index and the ionospheric indices/parameters TEC , $DROTI$, $S4$, and $\sigma\phi$ were compared during the geomagnetic storm conditions. The ionospheric scintillations are considered to be more typical for high and low latitudes. Mid-latitude scintillations are supposed to occur much less often. Here, first, we analyze the data of the mid-latitude station where the scintillation detection is a rather challenging problem and estimate the indices performance. Then we consider the example of high latitudes.

The 50 Hz $L1$ and $L2$ GPS data were obtained at the mid-latitude station ISTP (Irkutsk, Russia, geographic coordinates 52° N, 104° E) equipped with JAVAD GNSS receiver. The station is a part of SibNet network [25, 26].

As the de-trended TEC data is used to calculate $DROTI$ indices, the uncalibrated code-leveled phase TEC time series were derived from GPS phase and code measurements for this study. The phase TEC time series were de-trended by the centered moving window with 30 second accumulation time. $DROTI$ values were calculated from the de-trended 50 Hz TEC data with 1 second time resolution based on [5]. The indices $S4$ and $\sigma\phi$ were calculated from the de-trended 50 Hz $L1$ data based on the standard procedure [6] with 1 second time resolution as well.

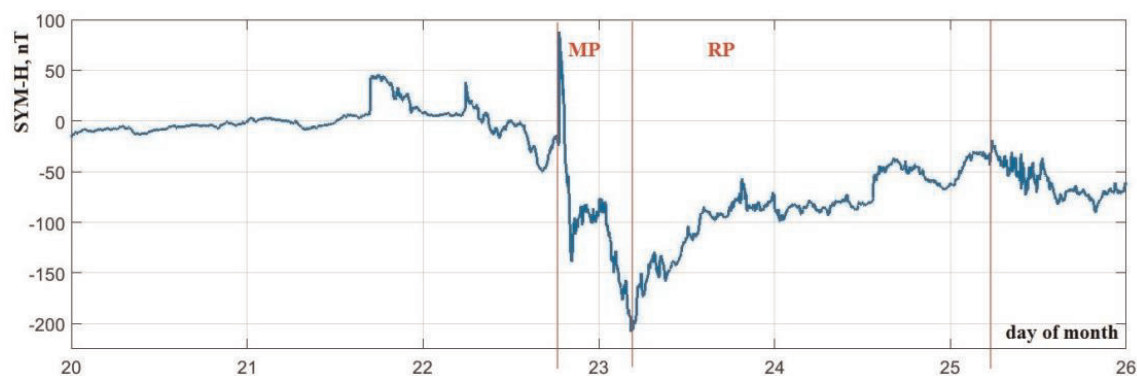


Figure 3. SYM-H variations during June 20–25, 2015. The MP and RP are indicated with the vertical red lines.

The storm period was chosen for the analysis as geomagnetic storms are known to cause ionospheric disturbances including the small-scale disturbances that are of the particular interest for this work. The intense storm of June 22–25, 2015, was under analysis. **Figure 3** shows SYM-H index variations during the storm. Main phase (MP) and recovery phase (RP) of the storm are marked with red lines [27]. SYM-H reached its minimum on June 23rd. SYM-H index data was obtained from Data Analysis Center for Geomagnetism and Space Magnetism following the link <http://wdc.kugi.kyoto-u.ac.jp/aeasy/index.html> (last access: August 2018).

According to [3], the relationship between $S4$, $\sigma\phi$, and $DROTI$ is complex, but in most cases the $S4$ increase means $DROTI$ increase and vice versa. **Figure 4** shows variations of the D2fi index, $DROTI$, $S4$, and $\sigma\phi$ indices during the storm for the GPS satellites PRN 04, PRN 15, and PRN 27 observed at ISTP station. Good

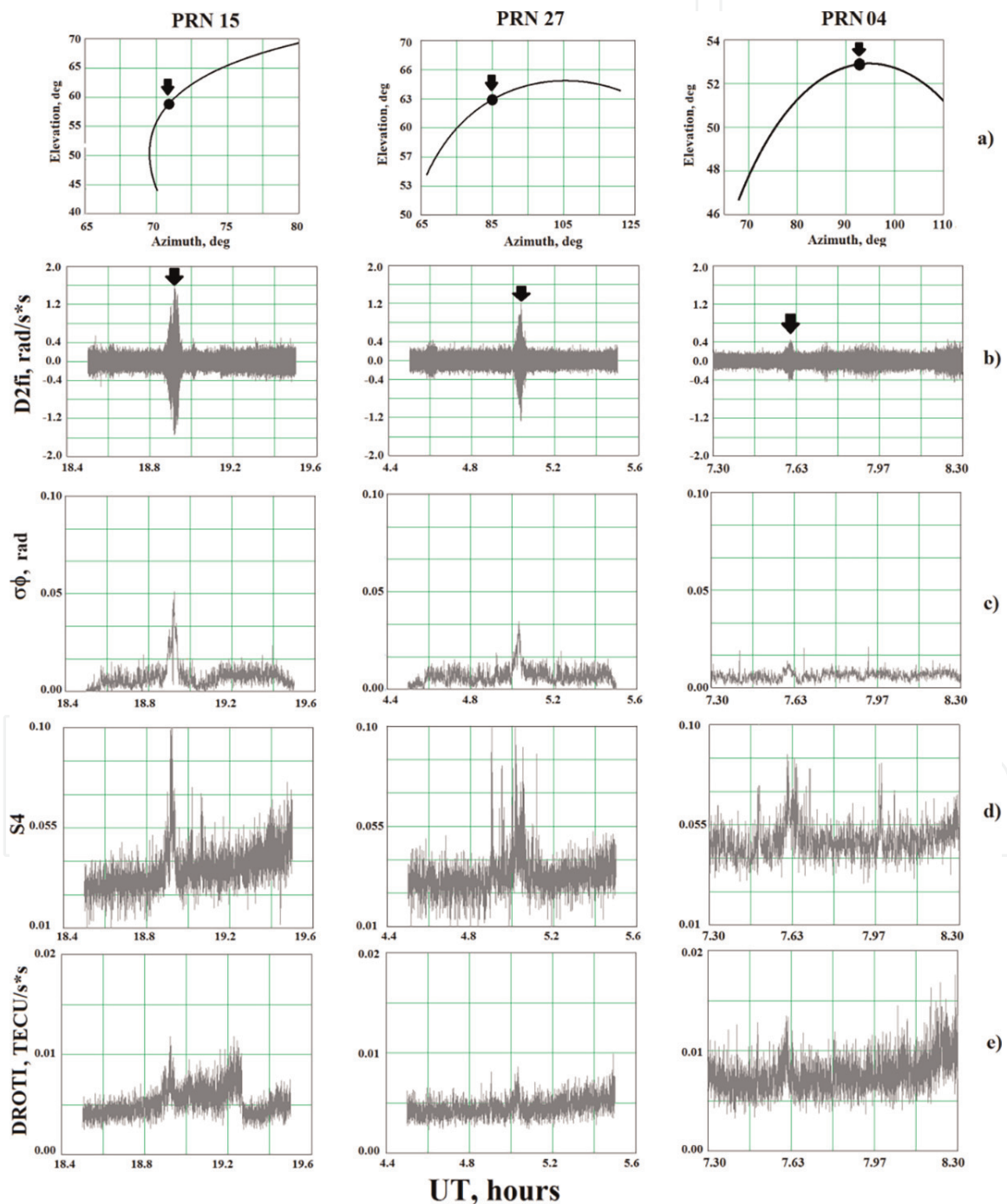


Figure 4. Time behavior of D2fi and standard scintillation indices. The dots indicate the approximate SV angular positions when the scintillation events were observed. (a) Elevation of the satellites, (b) D2fi, (c) $\sigma\phi$, (d) $S4$ and (e) $DROTI$.

correlation between the D2fi index and $\sigma\phi$ variations is seen for all the scintillation events and for all considered satellites, including the weakest event for PRN 04 (**Figure 4b** and **c**). Nevertheless, the peaks of the D2fi index are pronounced more sharply for all the cases. The correlation between the D2fi index and S4 variations is worse. There is a general similarity in behavior of these parameters, but S4 distribution is rather noisy and contains several peaks which do not coincide in time with the peaks of the D2fi index (**Figure 4b** and **d**).

The worst correlation is between the D2fi index and *DROTI* for all the cases under consideration (**Figure 4b** and **e**). The form of *DROTI* envelope significantly differs from the envelope of the D2fi index. To add, *DROTI* observations are rather noisy. Almost no *DROTI* response is seen for the SV PRN 27 (**Figure 4e**, middle panel). The small-scale ionospheric irregularities do not provoke significant TEC response [28]. Consequently, even weaker response can be expected in TEC-derived indices like *DROTI*, which is probably the case of **Figure 4e**.

Let us consider the advantages of the D2fi index in comparison to other indices by the example in **Figure 4**. First, it marks the sharper and more precise in time response to small-scale turbulences than other indices. Furthermore, only one GPS frequency is needed to obtain the D2fi index. Thus, it avoids the possible impact from the inter-frequency noises and *L1*-aiding technique features [23]. Third, as the D2fi index is calculated from either *L1* or *L2* phase data, it does not require any additional preprocessing and does not depend on the data processing technique [8]. Finally, another advantage of the D2fi index is its high sensitivity. We recall that mid-latitudes are usually considered as the region where the scintillation occurrence is null except during geomagnetic disturbances. Even for the presented case, the scintillation intensity is very low (S4 is not higher than 0.1, **Figure 4d**). Nevertheless, the D2fi index response on these scintillation events is clear, and it is more precise in time than other scintillation indices under consideration.

Now, let us consider the data from high-latitude region, where scintillations are more frequent. **Figures 5** and **6** are similar to **Figure 4** and show the results derived from the 50-Hz data at stations EDM (53,35° N, 247,02° W) and GJO (68,63° N, 254,15° W). Both stations belong to the Canadian High Arctic Ionospheric Network (CHAIN) [29] and equipped with the same type SEPTENTRIO PolaRxS GNSS receivers [30]. The station EDM is still within mid-latitudes (however in Canada it strictly depends on current geomagnetic conditions), but the station GJO is in high-latitude region.

The scintillation events are detected at both sites in the same time interval by all the considered indices: at EDM with PRN 30, PRN 26, and PRN 15 (**Figure 5**) and at GJO with PRN 06 (**Figure 6**).

It is seen that the weaker scintillation, the weaker the response of D2fi and $\sigma\phi$, which is not surprising as both indices are calculated from the same phase ranging data. Note that $\sigma\phi$ index quality depends on the phase de-trending and filtering procedure. This could bring the artificial effect that is seen at 19.87 UT at **Figure 6c** (left column).

The comparison of different indices allows us to reveal the prevalence of phase or amplitude scintillations. In our case (**Figure 5**) the obvious difference in S4 and $\sigma\phi$ behavior is seen for PRN 30, PRN 26, and PRN 15. Amplitude scintillations prevail at the ray path from PRN 30 (S4 exceeds 0.15, **Figure 5c**). On the other hand, phase scintillations are predominant at the ray paths from PRN 26 and 15 ($\sigma\phi$ index reaches 0.2 but S4 index does not exceed 0.02 at the same time).

To sum up, **Figures 4–6** prove the following: (a) D2fi peaks are caused by scintillation events (as there are also responses in other scintillation indices though less precise) and (b) that the D2fi index shows more sensitivity to phase scintillations.

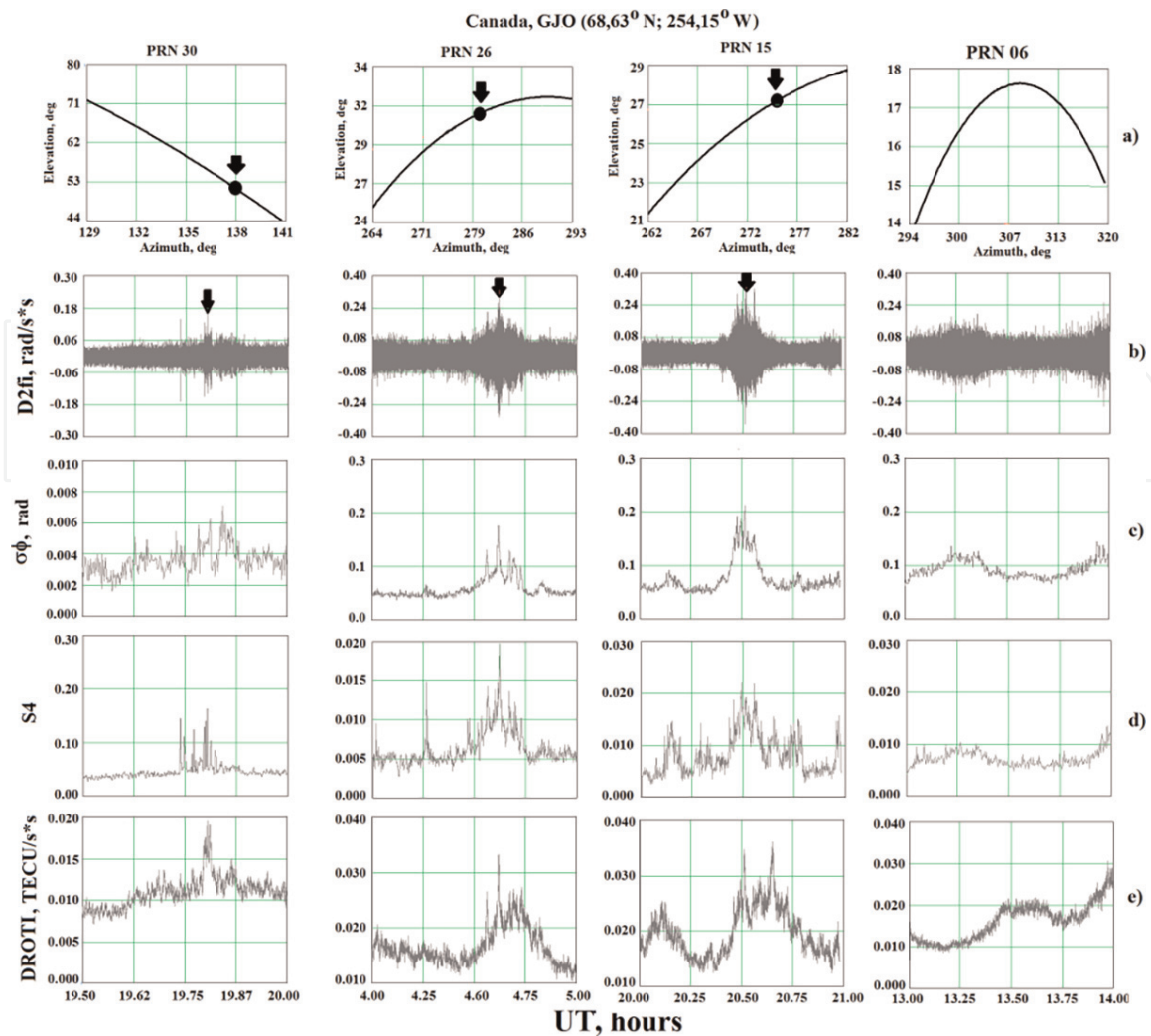


Figure 5.
 The same as in **Figure 4**, but for the high-latitude GJO station (Canada).

3.2 Time resolution comparison

The time resolution of input data is very important to detect scintillations. For example, the work [12] showed the significant sampling rate influence on *ROTI*. Indeed, the minimal size of the refractive irregularities is about the first Fresnel zone size (300–400 m at GNSS frequencies band). Such irregularities can cause both refractive and diffractive variations not only in the input carrier phase data but also in the ionospheric TEC and its derivatives as well as variations of *S4* and $\sigma\phi$ indices which are calculated based on 0.1–10 Hz data.

The smaller irregularities (from tens of meters to 100–300 m) are mostly considered to provoke the diffractive amplitude and phase variations. To detect them the highest time rate possible is needed (higher than 10 Hz). Diffractive phenomena can cause the phase scintillations that are usually accompanied by the intense amplitude fluctuations. These can be detected by $\sigma\phi$ and *S4* indices. When the diffractive Fresnel irregularities dominate, *CNR* and/or *S4* can vary significantly and show high correlation with $\sigma\phi$ [3].

Several kilometer size irregularities usually cause the refractive scintillations of 0.01–0.1 Hz. When such irregularities dominate, *S4* does not vary significantly and almost has no correlation to *ROTI*, *DROTI*, and even to $\sigma\phi$. Scintillations of refractive origin are better observed with the sharp TEC variations (i.e., by means of *ROTI* and *DROTI*) and with $\sigma\phi$ [3, 5]. There are studies focused on the scintillation

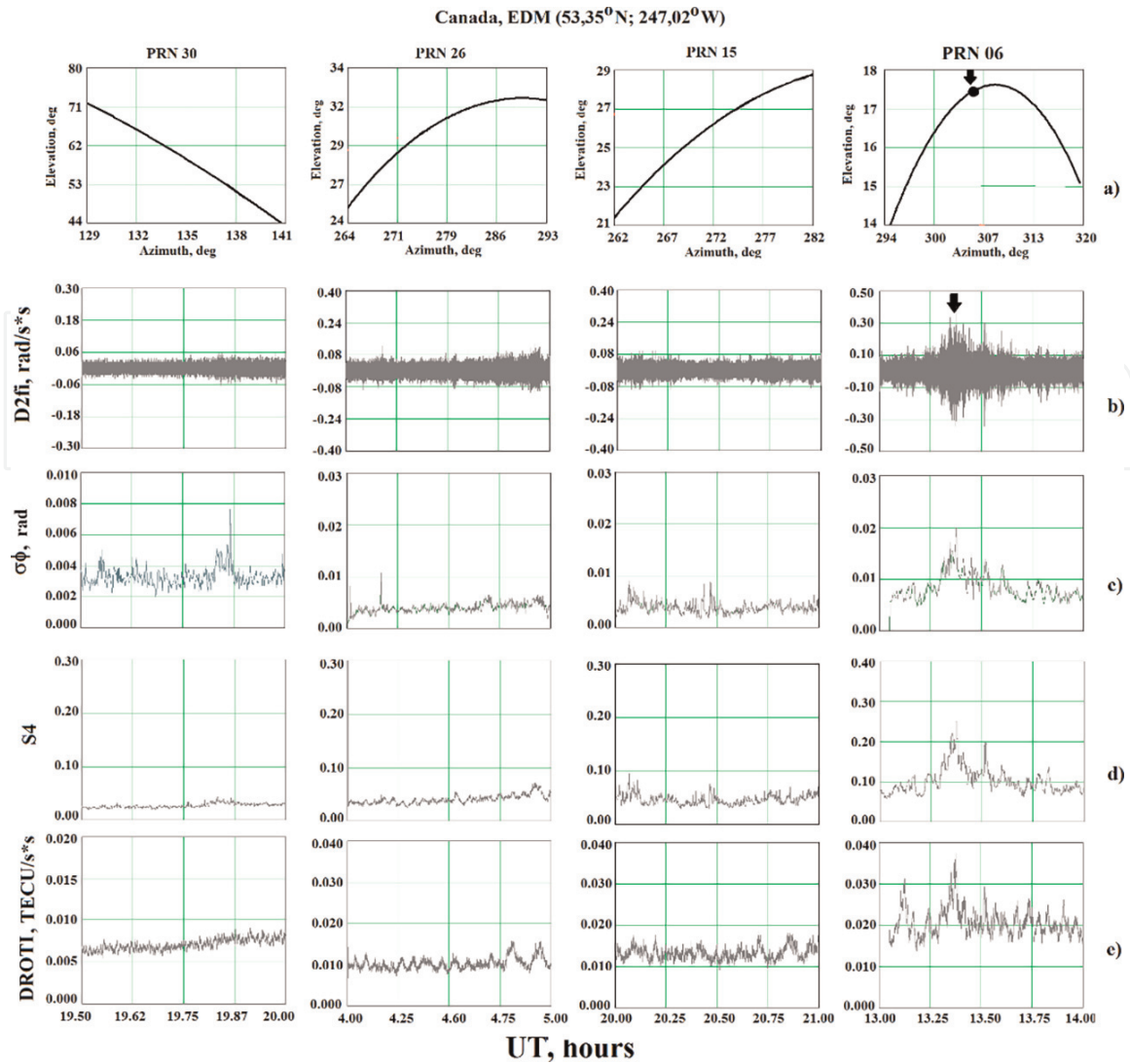


Figure 6.
 The same as in **Figure 4**, but for the high-latitude EDM station (Canada).

indices use based on the data of high-latitude receivers. For instance, the sDPR index was introduced in [15].

Usually, the irregularities of different scales are present in the ionosphere simultaneously. It can occur during the volcanic eruptions, powerful explosions, rocket launching, under disturbed geomagnetic conditions, etc. [4]. The ionospheric irregularities can move with the quiet different velocities and in different directions. The 1 Hz or lower time resolution data does not allow us to reveal if the ionospheric event was caused by the diffractive irregularities of hundreds of meters or by the larger refractive irregularities of tens of kilometers.

We suggest that the high data sampling rate such as 10 Hz and higher provides the opportunity to reveal and analyze the weak small-scale ionospheric irregularities. To test this assumption, we compared 1, 10, and 50 Hz time series of the D2fi index for the same events and under the same geomagnetic storm conditions.

Figure 7 shows the results of comparison for PRN 04, PRN15, and PRN27 at ISTEP station on June 22, 2015, during the main phase of the geomagnetic storm (**Figure 3**).

The D2fi index obtained from 1 Hz GPS data does not reveal any scintillation event for all three satellites (**Figure 7c**). In contrast, the time series obtained from 10 Hz data show the clear peaks for the SV PRN 15 and PRN 27 (**Figure 7b**), but not for the weakest event for SV PRN 04 (**Figure 7b**, left). The peaks of 50 Hz time series are the most pronounced for all the satellites (**Figure 7a**). Note that the 1 Hz

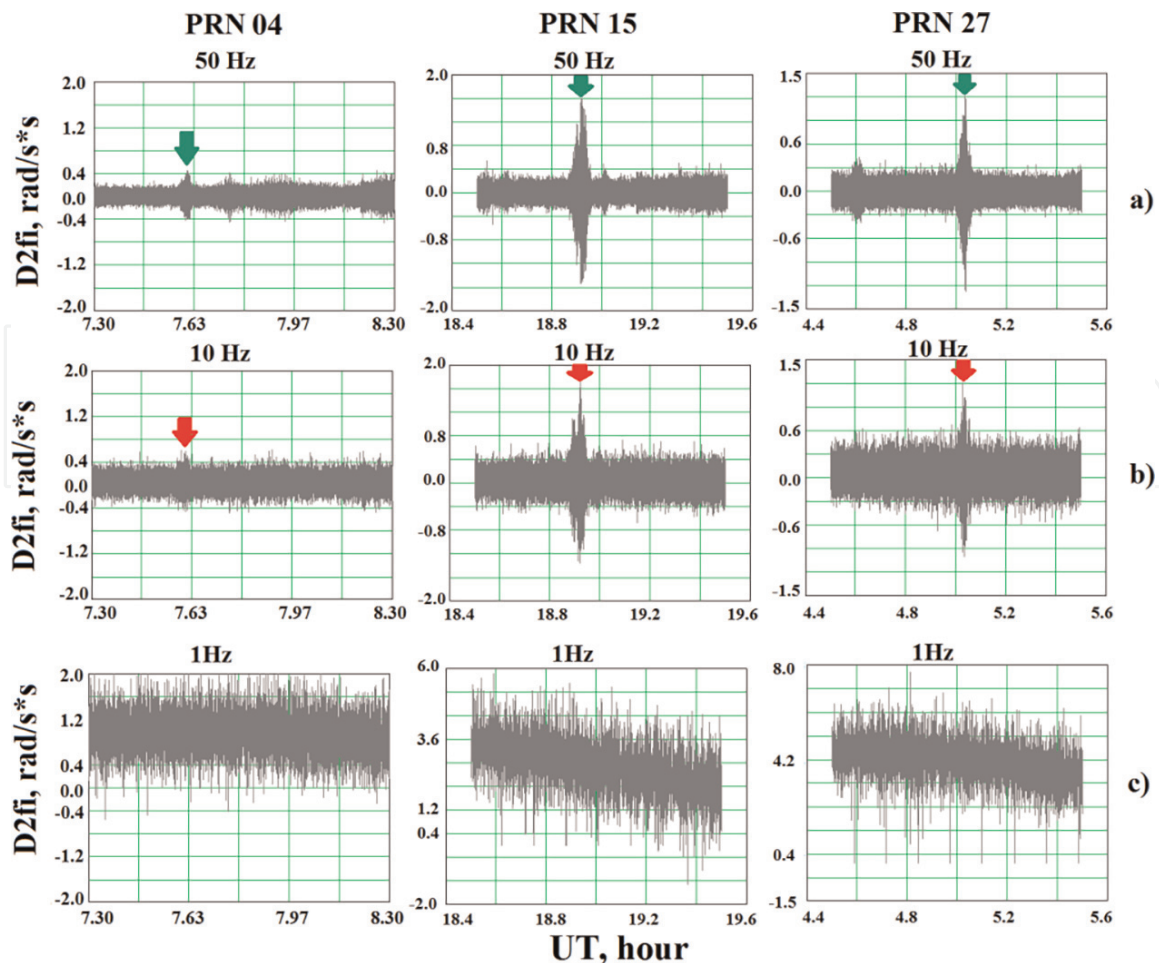


Figure 7. The $D2f_i$ index in case of 50 Hz data sampling rate (a), 10 Hz data sampling rate (b), and 1 Hz data sampling rate (c) for PRN 04, PRN 15, and PRN 27 on June 22, 2015, at ISTP station.

data shows both the highest noise level and the additional regular trend. The low-frequency trends are mostly removed from the time series of higher sampling rate.

In case of the highest data rate (50 Hz), the background values of $D2f_i$ do not exceed 0.4 rad/s*s (**Figure 7a**). For the lower data rate (10 Hz), the weak regular trend appears, and the background noise increases to 0.6 rad/s*s (**Figure 7b**). The $D2f_i$ variations increase 4–5 times and exceed 2–3 rad/s*s in the last case (1 Hz data, **Figure 7c**).

Apart from the ionospheric scintillations, one of the common sources of the phase fluctuations is the multipath effect. The majority of the multipath-induced fluctuations are observed at lower elevation angles. It is also not a thorough determination of multipath as it is possible to observe it at the higher elevations as well [1]. Thus, we should test if the scintillation events revealed above are related to multipath and/or blocked signal effects. Usually, the multipath-induced phase variations are caused by the repeating events due to local reflection or diffuse scattering. The picture of such events repeats from day to day at the same location. At the same time, the picture of such “scintillations” has the regular time shift about 16 s from one day to another due to GPS orbits daily motion [17]. This means that to determine whether the scintillation candidate events are caused by repeating local multipath effects, the raw data for the day before and after the scintillation should be analyzed. **Figure 8** illustrates such the analysis for 50 Hz data on June 21, June 22, and June 23, 2015, for PRN 04, PRN15, and PRN27.

No significant phase scintillations on the day before (June 21, **Figure 8**, left column) and/or after (June 23, **Figure 8**, right column) were observed. In contrast, there were the sharp and rapid variations of the second-order derivative of the

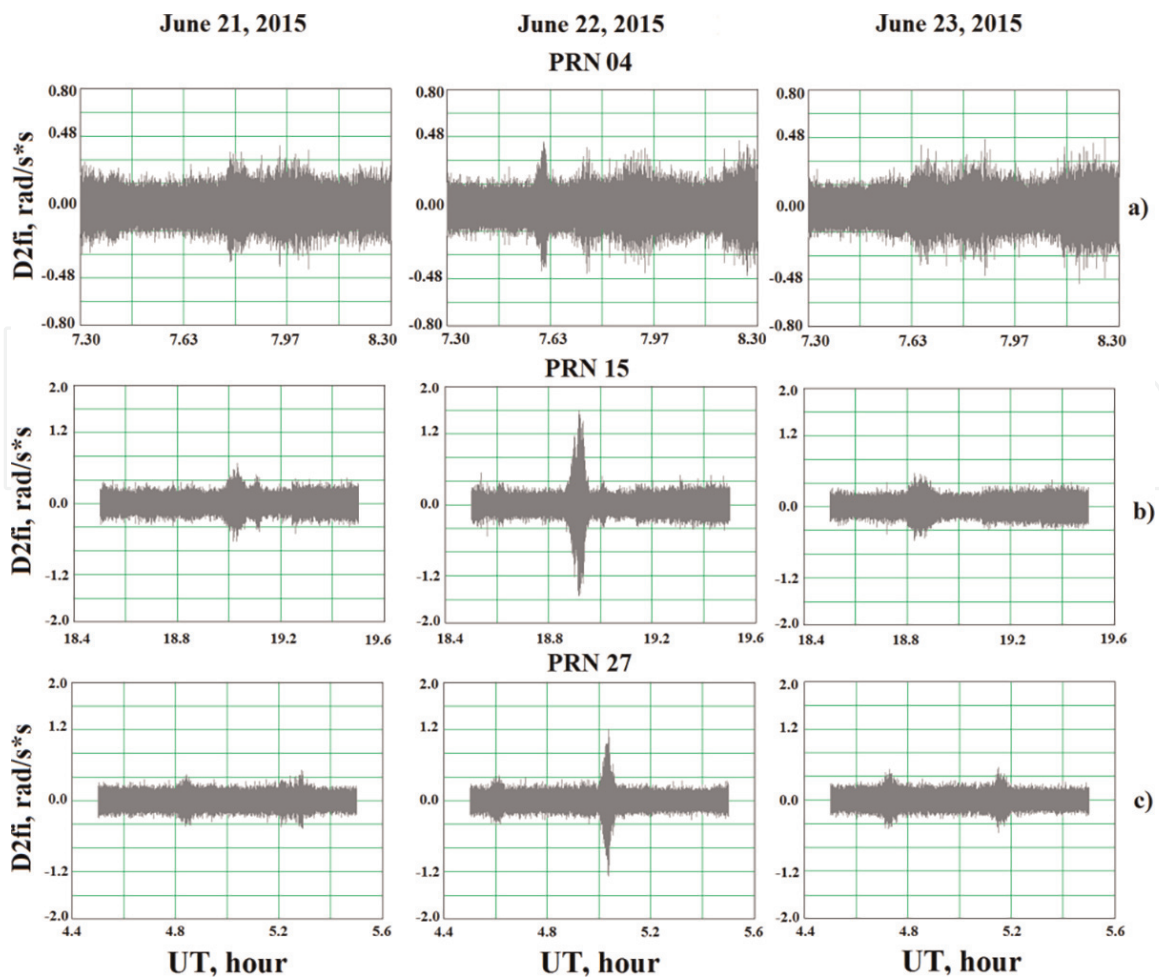


Figure 8.
 The $D2f_i$ index during June 21–23, 2015, for satellites PRN04 (a), PRN15 (b), PRN27 (c).

carrier phase on June 22, 2015, for all the satellites. This fact proves that the phase scintillation events observed on June 22, 2015, are not related to the multipath effect. Thus, the above mentioned phase scintillation events probably have the ionospheric origin.

4. Conclusions

The performance of the well-known “standard” ionospheric scintillation indices ROTI, DROTI, $S4$, $\sigma\phi$, and the new scintillation index $D2f_i$ that is the second-order derivative of the GPS signal carrier phase was analyzed in this study. The features of GNSS receivers and antennas that can have an effect on this performance were considered. The benefits and limitations of the indices were discussed.

The overall accuracy of the GNSS carrier phase measurements is limited by both thermal and external noises and significantly depends on the GNSS hardware and software presets and architecture. The accuracy of the carrier phase measurements can be improved if the particular specification is used for GNSS equipment suggested for the ionospheric studies. This particular specification means that the narrowband code delay discriminator, the large code rate for the open-access GNSS signals, the expanded front-end bandpass of the RFC, the low-noise preamplifier, and the specific pattern antenna should be specified for the ionospheric study.

In the present study, the new index $D2f_i$ is proved to be an effective tool to detect the small-scale ionospheric irregularities. It was shown that the sensitivity of the $D2f_i$ index depends on the data sampling rate. The higher the sampling rate, the

clearer the peaks of the D2fi index, and the weaker both the noise background and the low-frequency trend. The comparison between the D2fi index and DROTI, S4, and $\sigma\phi$ showed that they have different “sensitivities.” Each index has its own “critical” sensitivity for the particular ionospheric turbulences depending on the data sampling rate and preprocessing procedures. The advantage of the new D2fi index is that it is easily derived from the single-frequency carrier phase data. It provides both the reliable detection of the ionospheric scintillation and the phase time series de-trending with no complex data preprocessing. The new index can be applied as an independent scintillation indicator or as an additional tool together with other scintillation indices.

Acknowledgements

This work was supported by the Russian Federation President Grant No. MK-3265.2019.5 and by grant No. 18-05-00343 from the Russian Foundation for Basic Research. LANCE acknowledges partial support from CONACyT LN-299022, CONACyT PN 2015-173, and CONACyT-AEM Grant 2017-2101-292684. ISTP station data were recorded by the Angara Multiaccess Center facilities (<http://ckp-angara.iszf.irk.ru>) at ISTP SB RAS within the base financing of FR program II.16.

Conflict of interest

Vladislav Demyanov is the principal author and the corresponding author of this book chapter. The text and the figures presented in this book chapter were not published anywhere else before.

Author details

Vladislav V. Demyanov^{1*}, Maria A. Sergeeva^{2,3}
and Anna S. Yasyukevich¹


¹ Laboratory of Elaboration of New Methods for Atmosphere Radio Diagnostics, Institute of Solar-Terrestrial Physics, Irkutsk, Russia

² SCIESMEX, LANCE, Instituto de Geofísica, Unidad Michoacan, Universidad Nacional Autónoma de México, Michoacan, México

³ CONACYT, Instituto de Geofísica, Unidad Michoacan, Universidad Nacional Autónoma de México, Michoacan, México

*Address all correspondence to: vv.emyanov@gmail.com

IntechOpen

© 2019 The Author(s). Licensee IntechOpen. This chapter is distributed under the terms of the Creative Commons Attribution License (<http://creativecommons.org/licenses/by/3.0>), which permits unrestricted use, distribution, and reproduction in any medium, provided the original work is properly cited. 

References

- [1] McCaffrey AM, Jayachandran PT. Spectral characteristics of auroral region scintillation using 100 Hz sampling. *GPS Solutions*. 2017;**21**:1883-1894. DOI: 10.1007/s10291-017-0664-z
- [2] Fanis M, Stathis S. PLL bandwidth and noise in 100 Hz GPS measurements. *GPS Solutions*. 2015;**19**:173-185. DOI: 10.1007/s10291-014-0378-4
- [3] Bhattacharyya A, Yen KC, Franke SJ. Deducing turbulence parameters from transionospheric scintillation measurements. *Space Science Reviews*. 1992;**61**:335-386
- [4] Afraimovich EL, Perevalova NP, editors. *GPS-Monitoring of Earth Upper Atmosphere*. Irkutsk: Russian Academy of Sciences, Siberian Branch; 2006. 460p. ISBN 5-98277-033-7
- [5] Pi X, Mannucci AJ, Lindqwister UJ, Ho CM. Monitoring of global ionospheric irregularities using the worldwide GPS-network. *Geophysical Research Letters*. 1997;**24**:2283-2286. DOI: 10.1029/97GL02273
- [6] Van Dierendonck AJ, Klobuchar J, Hua Q. Ionospheric scintillation monitoring using commercial single frequency C/A code receivers. In: *Proceedings of ION GPS 1993*; Salt Lake City, Utah. 1993. pp. 1333-1342
- [7] Ghoddousi-Fard R. Impact of receiver and constellation on high rate GNSS phase rate measurements to monitor ionospheric irregularities. *Advances in Space Research*. 2017; **60**(9):1968-1977
- [8] Mushini SC, Jayachandran PT, Langley RB, MacDougall JW, Pokhotelov D. Improved amplitude-and phase-scintillation indices derived from wavelet detrended high-latitude GPS data. *GPS Solutions*. 2012;**16**(3):363-373
- [9] Priyadarshi S, Zhang QH, Thomas EG, Spogli L, Cesaroni C. Polar traveling ionospheric disturbances inferred with the B-spline method and associated scintillations in the southern hemisphere. *Advances in Space Research*. 2018;**62**(11):3249-3266
- [10] Jayanta KR. Mitigation of GPS code and carrier phase multipath effects using a multi-antenna system [thesis]. Calgary, Alberta: The University of Calgary; 2000
- [11] Qiongqiong J, Renbiao W, Wenyi W, Dan L, Lu W, Jie L. Multipath interference mitigation in GNSS via WRELAX. *GPS Solutions*. 2017;**21**:487-498. DOI: 10.1007/s10291-016-0538-9
- [12] Jacobsen KS. The impact of different sampling rates and calculation time intervals on ROTI values. *Journal of Space Weather Space Climate*. 2014;**4**: A33. DOI: 10.1051/swsc/2014031
- [13] Ledvina BM, Makela JJ, Kintner PM. First observations of intense GPS L1 amplitude scintillations at midlatitude. *Geophysical Research Letters*. 2002;**29**(14):4. DOI: 10.1029/2002GL014770. Available from: <https://agupubs.onlinelibrary.wiley.com/doi/epdf/10.1029/2002GL014770>
- [14] Kintner PM, Kil H, de Paula E. Fading time scales associated with GPS signals and potential consequences. *Radio Science*. 2001;**36**(4):731-743
- [15] Ghoddousi-Fard R, Prikryl P, Lahaye F. GPS phase difference variation statistics: A comparison between phase scintillation index and proxy indices. *Advances in Space Research*. 2013;**52**(8):1397-1405
- [16] Pavelyev AG, Liou YA, Wickert J, Schmidt T, Pavelyev AA. Phase

acceleration: A new important parameter in GPS occultation technology. *GPS Solutions*. 2010;**14**:3-11

[17] Kaplan ED. *Understanding GPS: Principles and Applications*. Boston, USA and London, UK: Artech House; 1996. p. 556

[18] MOPS Based Procedure for Minimum Recommended Testing of LightSquared RFI to GPS Aviation Receivers: Appendix A. 2017; p. 220. Available from: <https://ecfsapi.fcc.gov/file/7021690472.pdf>

[19] Global Positioning Systems Directorate Systems Engineering and Integration Interface Specification: IS-GPS-200J. 2018. Electronic resource. Available from: <https://www.gps.gov/technical/icwg/IS-GPS-200J.pdf>

[20] Global Positioning System Wing Systems Engineering and Integration Interface Specification. IS-GPS-705, Revision A: Navstar GPS Space Segment/User Segment L5 Interfaces. 2010. Electronic resource. Available from: <https://www.gps.gov/technical/icwg/IS-GPS-705A.pdf>

[21] Tsui JB. *Fundamentals of Global Positioning System Receivers: A Software Approach*. 2nd ed. Hoboken, New Jersey, USA: John Wiley & Sons, Inc., Publication; 2005. 605p. ISBN 0-471-70647-7

[22] Van Nee R. Multipath effects on GPS code phase measurements. In: *Proceedings of ION GPS*. 1991. pp. 915-924

[23] Padma B, Kai B. Performance analysis of dual-frequency receiver using combinations of GPS L1, L5, and L2 civil signals. *Journal of Geodesy*. 2019;**93**:437-447. DOI: 10.1007/s00190-018-1172-9

[24] Braasch MS. GPS multipath model validation. In: *Proceedings of ION PLANS*. 1996. pp. 672-678

[25] Yasyukevich YV. 2017. The 50 Hz JAVAD Data Set for the Case Study. Available from: 10.5281/zenodo.848325 [Accessed May 30, 2019]

[26] Yasyukevich YuV, Vesnin AM, Perevalova NP. SibNet-Siberian global navigation satellite system network: Current state. *Solar-Terrestrial Physics*. 2018;**4**(4):63-72. DOI: 10.12737/stp-44201809

[27] Piersanti M, Alberti T, Bemporad A, Berrilli F, Bruno R, Capparelli V, et al. Comprehensive analysis of the geoeffective solar event of 21 June 2015: Effects on the magnetosphere, plasmasphere, and ionosphere systems. *Solar Physics*. 2017;**292**(11):169

[28] Perevalova NP, Sankov VA, Astafyeva EI, Zhupityaeva AS. Threshold magnitude for ionospheric TEC response to earthquakes. *Journal of Atmospheric and Solar-Terrestrial Physics*. 2014;**108**:77-90

[29] Jayachandran PT, Langley RB, MacDougall JW, Mushini SC, Pokhotelov D, Hamza AM, et al. The Canadian high arctic ionospheric network (CHAIN). *Radio Science*. 2009; **44**:RS0A03. DOI: 10.1029/2008RS004046

[30] Bougard B, Sleewaegen JM, Spogli L, Veetil SV, Monico JF. CIGALA: Challenging the solar maximum in Brazil with PolaRxS. In: *Proceedings of the 24th International Technical Meeting of the Satellite Division of the Institute of Navigation 2011, ION GNSS*. Vol. 2011. 2011. pp. 2572-2579